Role of electric currents for the SOL and divertor target heat fluxes in ASDEX Upgrade

D. Brida[1], D. Silvagni[1,2], T. Eich[1], M. Faitsch[1], P. McCarthy[3], the ASDEX Upgrade Team* , and the MST1 Team†

[1]Max-Planck-Institut für Plasmaphysik, Boltzmannstr. 2, 85748 Garching, Germany
[2]Physik-Department E28, Technische Universtität München, Boltzmannstr. 15, D-85748 Garching bei München
[3]Department of Physics, University College Cork, Cork,Ireland

June 26, 2020

Abstract

In divertor tokamaks electric currents flowing in the Scrape-Off Layer (SOL) are a frequently observed and well known feature. However, the convective heat flux carried by these currents is often assumed to be small compared to the total parallel heat flux. In this paper it is shown that in ASDEX Upgrade the electric current, which was measured by Langmuir probes at the outer target, can be several times larger than the ion saturation current in low density L- and H-mode discharges. Therefore they have to be taken into account when calculating the target heat flux from the Langmuir probe data. Moreover, a detailed analysis reveals that for low density L- and H-mode discharges the heat flux profile is mainly determined by the current profile. By applying a 1D heat flux transport model it is demonstrated that the electric current can carry a large fraction ($> 50\,\%$) of the electron heat flux along the SOL convectively. Thus a Spitzer-Härm approach, where it is assumed that heat is transported only conductively, might not be valid in the investigated regime.

*See author list of H. Meyer et al. 2019 Nucl. Fusion 59 112014
†See author list of B. Labit et al. 2019 Nucl. Fusion 59 086020

1 Introduction

In divertor tokamaks, such as the next step fusion device ITER, heat is transported across the separatrix and flows in the Scrape-Off-Layer (SOL) within a narrow channel [1] towards the inner and outer divertor targets. Due to a combination of drifts [2], geometry effects, and poloidally varying anomalous transport, the plasma tends have different temperatures at the two target plates. This temperature asymmetry drives a current carried by electrons flowing from the colder towards the hotter target along the SOL [3, 4], which will be called *thermoelectric current* in the following. The flow of electrons can contribute significantly to the parallel heat flux towards the hot plate, and thereby increase the already existing temperature asymmetry further [5, 6]. Analytical and numerical SOL models often neglect this contribution to the transport and assume that heat is carried only by conduction. Thus it is of high importance to know under which conditions this is valid.

SOL currents are investigated experimentally in several tokamaks. In Alcator C-Mod [7] and JET [8] electric currents larger than the ion saturation current were measured. By calculating the heat flux from LP measurements the authors showed that the currents contribute significiantly to the target heat flux. In ASDEX Upgrade (AUG) thermoelectric currents are known to occur [9], and their measurement by shunt resistors are useful to approximate the outer target electron temperature for detachment control [10].

In this study Langmuir Probe (LP) measurements of divertor target currents of AUG L- and H-mode discharges are presented and the implications for LP data analysis and for the heat flux transport are discussed. In section 2 the LP diagnostic setup and analysis are explained, and in section 3 the discharge setup and measurements are presented. The physical mechanism driving these currents and the dependence of the electric current on the density are discussed in section 5. In section 4 the heat flux profiles calculated from the Langmuir probe measurements are compared to infrared data, and the role of the current for the target heat flux is discussed. In section 6 a simplified model for the SOL heat transport with electric currents is solved for typical low density L- and H-mode conditions, and it is shown that a significant contribution of the heat can be carried by the electric current. In section 8 the results are summarized.

2 Diagnostic setup

The main diagnostics used for this study are the Langmuir probes in the lower divertor of AUG, which are displayed in Fig. 1 (a). The red dots at the outer target correspond to dome shaped single probes which have a radius of about 2.5 mm and are separated poloidally by about 2 cm. A triangular voltage signal is applied to them, i.e. they are *swept* to obtain current-voltage (IV) characteristics. The sweeping frequency is about 200 Hz. As an example in Fig. 1 (b) an IV characteristic taken in an L-mode discharge is shown. On the horizontal axis the applied voltage with respect to the target potential V_{tar}, and on the vertical axis the measured current is plotted. A model is fitted to the characteristic from which the electron temperature T_e and the ion saturation current density j_{sat} are obtained. The electric current density to the target j_{net} is calculated from the current drawn by the probe at $V = V_{\mathrm{tar}}$, i.e. when it is grounded. In this paper the following sign convention for the current densities is chosen: j_{net} is positive for a net electron current and negative for a net ion current towards the target. The ion saturation current density j_{sat} has a different sign, i.e. it is positive. This sign convention allows a more compact representation of j_{net} and j_{sat} profiles in the same plot.

The fitting model from [11] is used to describe the non saturation of the ion flux [12,13] due to the expansion of the Debye sheath with increasing probe voltage. Moreover a double probe characteristic is assumed to take into account the decreased electron saturation current which is typically observed at shallow magnetic field incidence angles [13, 14].

The black dots in Fig. 1 (a) correspond to flush mounted probes, which are toroidally displaced with respect to the dome shaped probes and have poloidal and toroidal extensions of about 5 and 25 mm, respectively. The flush mounted probes are commonly operated as triple probes [15] by which T_e and j_{sat} are obtained at a frequency of about 25 kHz. Since in a triple mode operation not the full IV characteristic is obtained, these fitted values are less reliable then the ones obtained by the swept probes. An additional grounded flush mounted probe can be used to obtain j_{net}. The data from the flush mounted probes are only used in section 5 to compare inner and outer target fluxes, whereas the data in the other sections are obtained from the dome shaped probes.

The non saturation of the ion flux depends on the probe geometry and the incident field line angle onto the probe [12, 13]. However, the non saturation effect should not play a role when the probe is at the same potential as the target, i.e. when the electric current is measured. Hence, the measurement of the electric current should be independent of the probe shape. In Fig. 2 the electric current density profiles obtained from swept flush and dome shaped

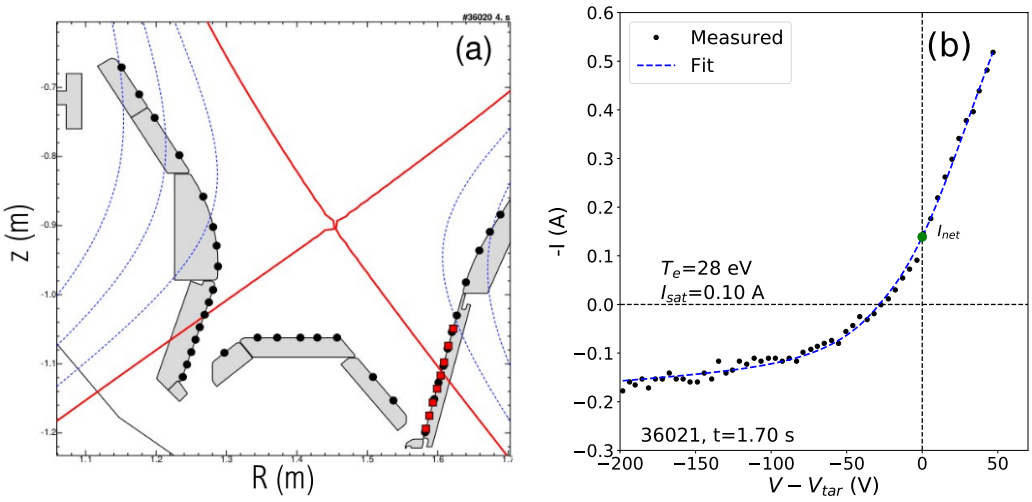

Figure 1: (a) Flush mounted (black) and dome (red) Langmuir probes in the lower divertor in AUG. (b) Typical current voltage characteristic for a dome shaped probe and corresponding fit for the AUG discharge 36020. I_{sat} and T_e are the ion saturation current and the temperature obtained from the fit, and I_{net} is the electric current.

probes in an L-mode during a strike line sweep are compared. The inclination angle between the probes and magnetic field was here about 2.5° for the flush probe and about 5° for the dome probe. The good agreement between the two measurements corroborates the assumption that the probe shape does not influence the electric current measurements.

The outer target is also observed by an IR camera to measure the target temperature with a time resolution of about 1 kHz [16]. The heat flux onto the divertor target is calculated from the temperature measurements using the implicit version [17] of the THEODOR code [18].

3 Discharge setups and current measurement results

In the following, two well diagnosed low collisionality deuterium L- and H-mode discharges and related LP measurements are discussed. We focus on low collisionality discharges because, as will be seen in Sec. 5 the SOL currents have the strongest effect on the target heat flux for an attached inner divertor. Moreover, studies on the heat flux width often focus on low collisionality discharges as well, since the target IR data is more reliable at low density and

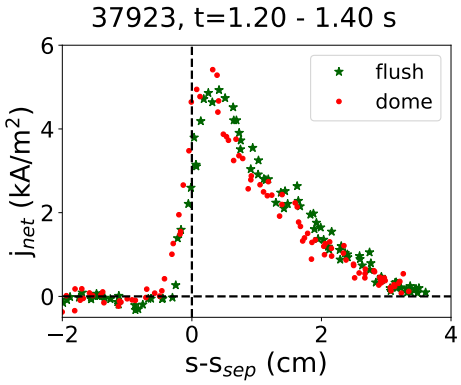

Figure 2: Electric current density profile j_{net} measured by flush and dome shaped probes during an L-mode discharge.

can be accurately described [19] in the absence of dissipation [20]. Therefore, the results presented here directly contribute to a better understanding of the divertor heat flux estimates in such low density discharges.

In both discharges the magnetic field is $B_t = -2.5\,\mathrm{T}$, and the ion ∇B drift is directed towards the active X-point, which is the standard direction for tokamak operation. With this setup the outer target tends to have a higher electron temperature than the inner one, i.e. the thermoelectric current is directed towards the inner divertor. For the case with a reversed magnetic field, i.e. with the ion ∇B drift directed away from the active X-point, it was shown that the temperature asymmetry between inner and outer divertors becomes smaller [21]. Therefore, it is expected that the standard magnetic field configuration shows larger thermoelectric currents than the reversed field configuration.

Figure 3 shows the time traces for the L-mode discharge 36280 of (a) the plasma current I_{p}, (b) the Electron Cyclotron Resonance Heating (ECRH), Neutral Beam Injection (NBI) and Ohmic heating powers P_{ECRH}, P_{NBI} and P_{OH}, (c) the density n_{H5} measured along the interferometry line of sight H5 [22] and (d) the strike point position at the outer target with respect to an arbitrarily chosen offset location. The line of sight H5 passes through the edge, n_{H5}, and is used as a measure for the edge density.

For the LP analysis the time range between 6.0 and 6.35 s is used, marked red in Fig. 3. In this time range the outer target strike point is moving by about 2.5 cm to obtain continuous LP profiles. The plasma current I_{p} decreases from 0.8 MA to about 0.75 MA during that time range. The edge density n_{H5} is about $0.9 \times 10^{19}\,\mathrm{m}^{-3}$ and $P_{\mathrm{ECRH}} = 0.4\,\mathrm{MW}$. Measurements by the edge Thomson scattering system show that the variation of I_{p} does

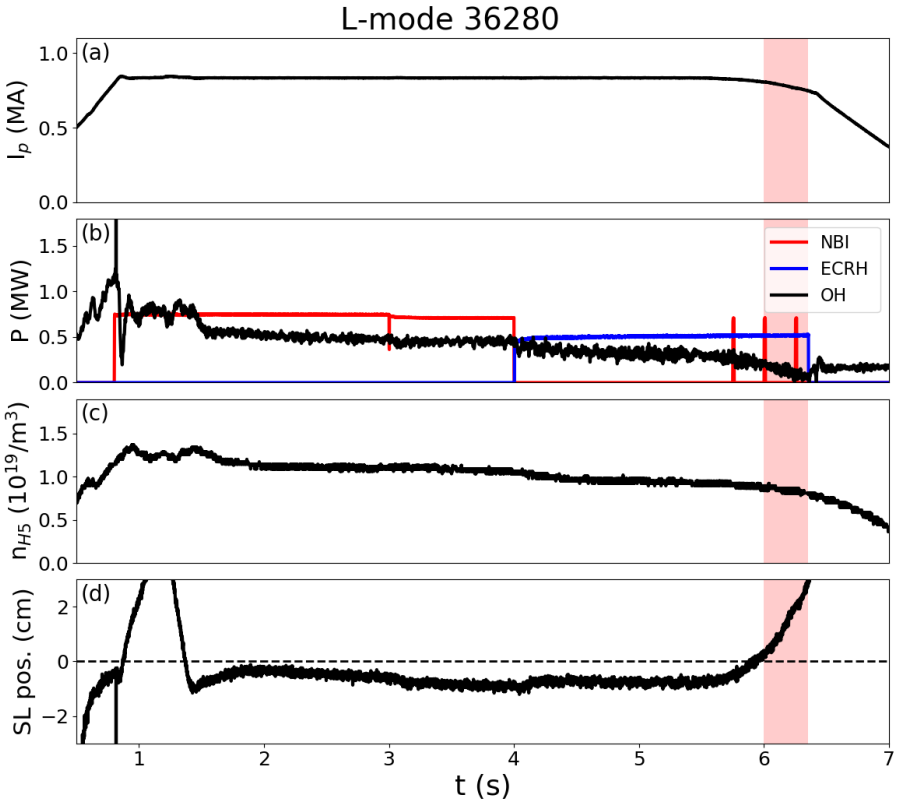

Figure 3: Time traces for AUG L-mode discharge 36280: (a) Plasma current I_p, (b) Ohmic power P_OH, NBI heating and ECRH heating powers P_NBI and P_ECRH, (c) edge density n_H5 from interferometry measurements, (d) outer divertor strike point position. The red region marks the time range where Langmuir probe data are analysed.

not affect the upstream density and electron temperature profiles within the measurement uncertainties.

The outer target profiles of j_sat and j_net are shown in Fig. 4 (a). Here s is the target coordinate and s_sep is the strike line location. The dots are the data obtained from individual IV curves and the solid lines polynomial fits to the data. The j_net profile shows a narrow width of about 1 cm and has a peak value of about 5 kA/m^2. Compared to j_sat it is very narrow and about three times higher in peak value. The electron temperature T_e is shown in Fig. 4 (b). The peak value of T_e is about 60 eV. This might be an overestimation of the actual value, as the fitted parameters become more uncertain at high electron temperatures. Furthermore, an underestimation of the non saturation of the ion flux can as well lead to an overestimation of

T_e [23].

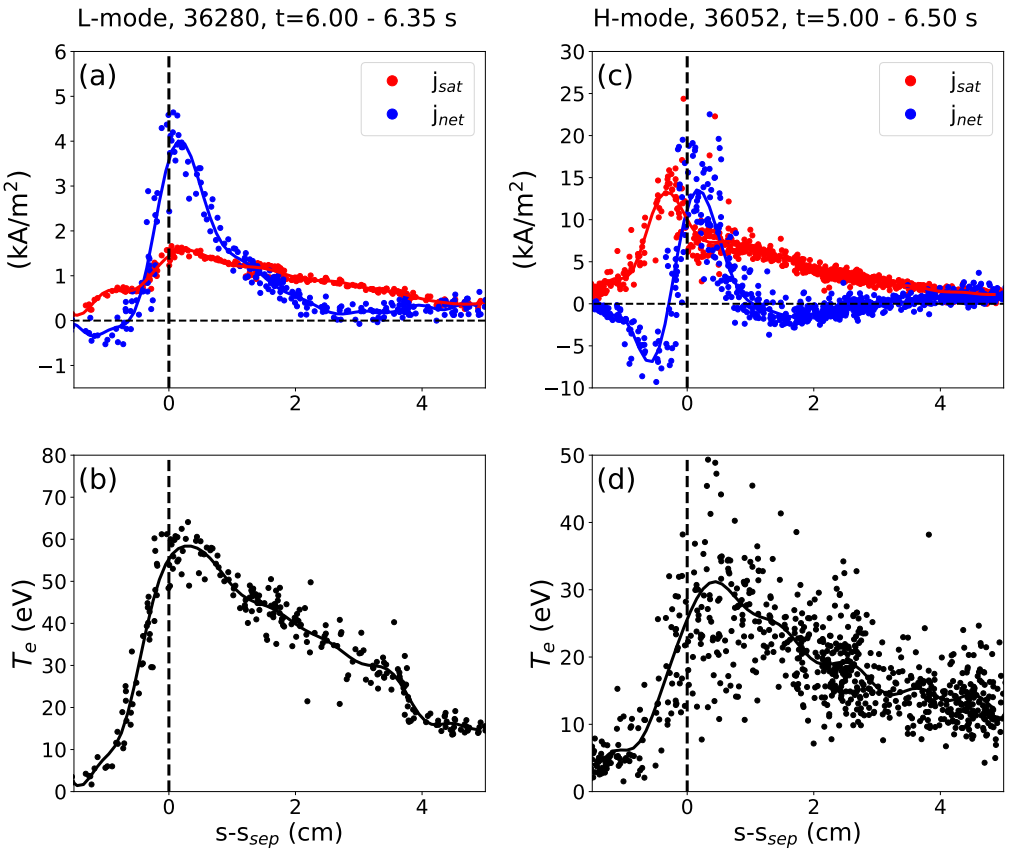

Figure 4: (a+c) Outer target ion saturation and electric current profiles j_{sat} and j_{net} and (b+d) electron temperature profiles T_e for the AUG L-mode discharge 36280 and the H-mode discharge 36052.

The time traces for the H-mode discharge 36052 are shown in Fig. 5. The time range used for the LP profiles is between 5.0 and 6.5 s, indicated by the red shaded region. In Fig. 5 (d) the outer target strike point position is shown. In this time range a strike line sweep of about 4 cm is performed in order to obtain continuous probe profiles. The ELMs, which are clearly observed in P_{OH} and the strike line movement, appear at a low frequency of about 70 Hz. The long inter ELM phases of about 10 ms allow the analysis with swept probes. During the inter ELM phases the strike line position is still fluctuating with an amplitude of about 0.5 cm. This makes the data analysis close to the profile peaks where the decay lengths are about 1 cm challenging. In particular, this leads to a smoothing of the profiles around the peak position.

Figure 4 (c) shows the outer j_{net} and j_{sat} profiles and (d) the T_e profile for this discharge. In this case j_{net} has a peak value of about $15\,\mathrm{kA/m^2}$, which is about twice the value of j_{sat} at the same location, and becomes negative in the Private Flux Region (PFR). The dip of j_{net} in the PFR is explained by the diamagnetic current across the divertor leg due to the poloidal pressure gradient [2, 24, 25]. To ensure that the electric current is divergence free, it must then flow along the field lines towards the target.

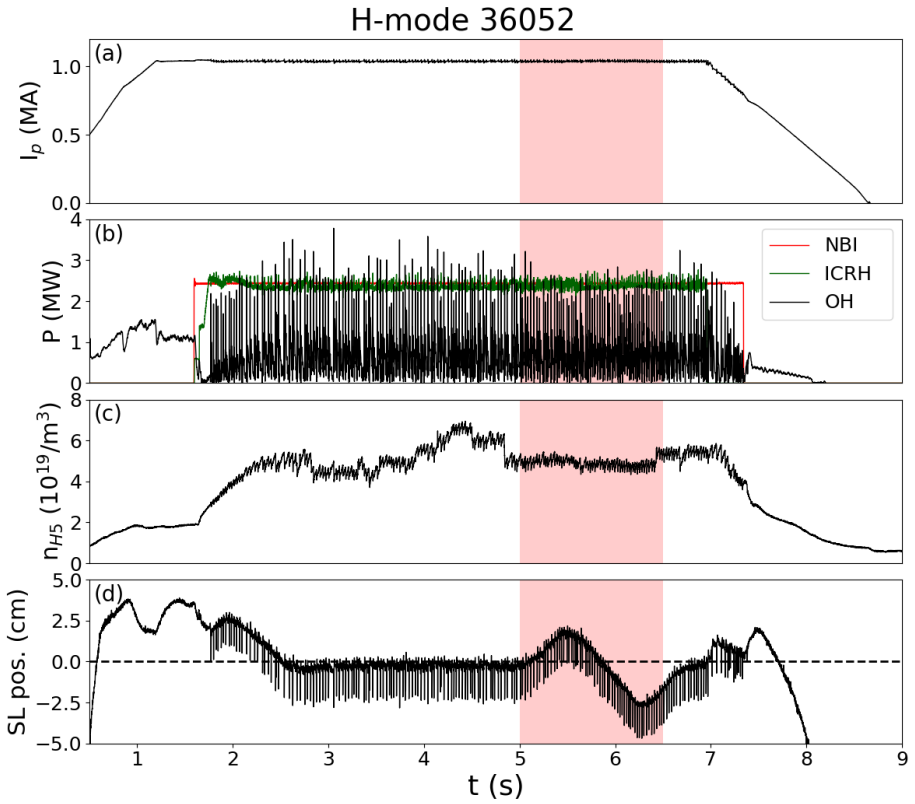

Figure 5: Time traces for AUG H-mode discharge 36052: (a) Plasma current I_{p}, (b) Ohmic power P_{OH}, NBI and ICRH heating powers P_{NBI} and P_{ICRH}, (c) edge density n_{H5} from interferometry measurements, (d) outer divertor strike point position. The red region marks the time range where Langmuir probe data are analysed.

4 Target heat flux calculation from LP measurements and comparison to infrared data

The fact that the outer target currents can be significantly higher than the saturation current is crucial for the interpretation of target heat flux profiles. This will be demonstrated in this section by analysing the heat flux profiles of the two L- and H-mode discharges discussed in section 3. From sheath theory [26] it is well known that, assuming equal electron and ion temperatures, about 2/3 of the heat flux is transmitted by the ions to the target for ambipolar conditions, i.e. for $j_{\mathrm{net}} = 0$. This, however, is not valid for strongly non-ambipolar conditions.

The individual heat flux contributions are calculated from LP measurements by decomposing the total heat flux according to the model described in [26], chapter 25.5:

$$q_{\mathrm{mod}} = q_e + q_i + q_{\mathrm{rec}}, \tag{1}$$

with

$$q_e = 2T_e(j_{\mathrm{sat}} + j_{\mathrm{net}}),\ q_i = (2.5T_i + eV_{\mathrm{sh}})(1 - R_E)j_{\mathrm{sat}} \text{ and } q_{\mathrm{rec}} = E_{\mathrm{rec}}j_{\mathrm{sat}} \tag{2}$$

Here q_e and q_i are the electron and ion contributions and q_{rec} the energy deposited due to recombination at the target surface. T_i is the ion temperature, V_{sh} the potential drop in the sheath forming in front of the target, R_E the ion energy reflection coefficient [27], and $E_{\mathrm{rec}} = 13.6\,\mathrm{eV}$ the recombination energy per impinging ion. Secondary electron emission has been neglected due to the prompt redeposition of electrons at small magnetic field incidence angles [28].

The sheath potential drop is calculated according to

$$V_{\mathrm{sh}} = \overbrace{-0.5\ln\left[2\pi\frac{m_e}{m_i}\left(1+\frac{T_i}{T_e}\right)\right]T_e}^{V_{\mathrm{pl,fl}}} + \overbrace{\ln\left(\frac{j_{\mathrm{net}}}{j_{\mathrm{sat}}}+1\right)T_e}^{V_{\mathrm{tar,fl}}}, \tag{3}$$

where the term $V_{\mathrm{pl,fl}}$ is the difference between the plasma and the floating potential [26], and the second term $V_{\mathrm{tar,fl}}$ is the difference between the floating and the target potential. Since $-V_{\mathrm{tar,fl}}$ is approximately the voltage at which an LP draws zero current this term can also be read directly from LP measurements, as it is done in this study.

While the contributions q_e and q_{rec} are calculated directly from the LP measurements, this is not possible for q_i without further assumptions on T_i and R_E. R_E depends both on the ion incidence energy and angle as well as the surface material [27]. For ions impinging perpendicular to a

tungsten surface, and ion temperatures above 20 eV, an almost constant value of $R_E \approx 0.5$ is reported [27,29]. Due to a complete lack of information about the ion temperature, T_i is assumed to be between 0 and $2T_e$. This assumption should give a range of realistic ion heat fluxes.

It is common to express Eq. (1) in terms of ion and electron *sheath heat transmission factors* γ_i and γ_e, defined by [26]

$$\gamma_{i,e} = \frac{q_{i,e}}{j_{\mathrm{sat}} T_e} \tag{4}$$

For fixed R_E and T_i/T_e, the total sheath heat transmission factor $\gamma_{\mathrm{tot}} \equiv \gamma_i + \gamma_e$ is a function of the ratio $j_{\mathrm{net}}/j_{\mathrm{sat}}$. In Fig. 6 (a) γ_{tot}, γ_i and γ_e are plotted for the case $T_i = 0$. Here the convention from [26] was adopted to use $eV_{\mathrm{tar,fl}}/T_e$ as an independent variable. With increasing $eV_{\mathrm{tar,fl}}/T_e$, the sheath potential drop decreases (see Eq. (3)) and more electrons pass the sheath. As a consequence γ_e is increasing exponentially. The ion sheath heat transmission factor γ_i on the other hand is decreasing corresponding to a decreased energy gain of the ions in the sheath. The total sheath heat transmission factor γ_{tot} is 3.6 for $V_{\mathrm{tar,fl}} = 0$ and increases to about 6.6 at $eV_{\mathrm{tar,fl}}/T_e = 1$, which corresponds to the case $j_{\mathrm{net}}/j_{\mathrm{sat}} \approx 3$. The sheath heat transmission coefficients for $T_i = 2T_e$ are shown in Fig. 6 (b). Due to the higher ion energies with respect to the case $T_i = 0$, the sheath heat transmission factor increases to 5.8 at $V_{\mathrm{tar,fl}} = 0$ and 8.8 at $eV_{\mathrm{tar,fl}}/T_e = 1$.

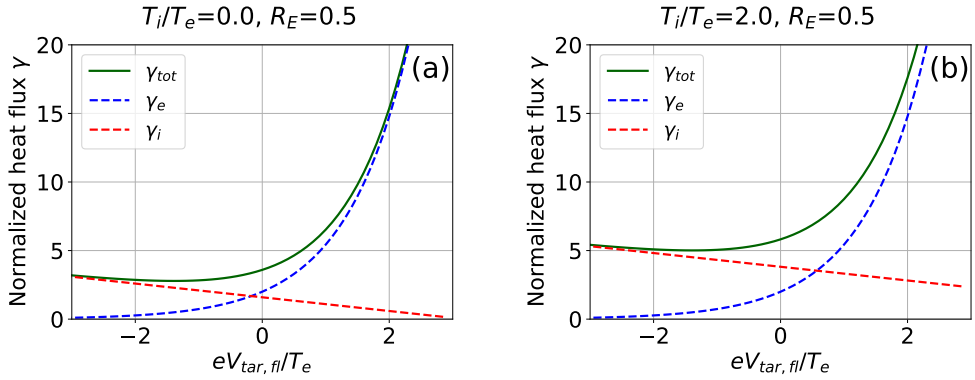

Figure 6: Electron, ion and total sheath heat transmission factors γ_e, γ_i and γ_{tot} in dependence of $eV_{\mathrm{tar,fl}}/T_e$ according to Eq. (1) for the assumption (a) $T_i = 0$, and (b) $T_i = 2T_e$. In both cases $R_E = 0.5$ is assumed.

The heat fluxes q_e, q_{rec} and q_i obtained for the L-mode discharge 36280 are shown in Fig. 7 (a). To obtain these profiles, the polynomial fits shown in Fig. 4 (a) were used for j_{sat}, j_{net} and T_e in Eq. (1). The dashed magenta

line shows the ion heat flux for the assumption $T_i = T_e$. The lower and upper boundaries of the shaded region correspond to the ion heat fluxes for $T_i = 0$ and $T_i = 2T_e$, respectively. The electron heat flux q_e is between 2 and 5 times larger than q_i, and has a several times shorter decay length. The recombination heat flux q_{rec} is negligible. The total heat fluxes q_{mod} is plotted in Fig. 7 (b) together with the heat flux q_{IR} obtained from IR measurements. A good agreement with q_{mod} is obtained for $s - s_{\mathrm{sep}} > 0$ for the whole range of assumed ion temperatures. Although q_{IR} tends to be below the q_{mod} obtained for $T_i = T_e$ it cannot be concluded that $T_i < T_e$, since the effect of T_i on the total heat flux is relatively small with respect to the uncertainties in the probe measurements and the IR data. In the PFR q_{IR} decays steeply, which is not seen in q_{mod}.

The heat flux profiles for the H-mode discharge 36052 are shown Fig. 7 (c) and (d). The obtained peak value of q_e is between one and three times that of q_i. Close to the peak value, where as discussed in section 3 the uncertainties are high, q_{IR} is underestimated.

The analysis made in this section shows that the heat flux decay length in the discussed cases is strongly determined by the electron heat flux decay length. The electron heat flux decay length, on the other hand, is mainly determined by the j_{net} profile. In section 5 is was furthermore shown that in low density L-mode plasmas the j_{net} profile is determined by the inner target saturation current profile, with additional contributions from the radial diamagnetic drift. Conclusively, the thermoelectric current leads to a coupling between the outer target heat flux and the inner target saturation current in low density discharges.

5 Change of outer target current through inner target conditions

The examples discussed so far in this paper demonstrate that electric currents several times larger than the ion saturation current can occur at the outer target and that this current can contribute significantly to the target heat flux. It is now shown that the electric current profile is largely explained by a thermoelectric effect. Furthermore, it is analysed how a change of the inner target conditions can affect the thermoelectric current.

For a floating target, i.e. if the current to the target is zero, the sheath potential is approximately proportional to the electron temperature. If the electron temperatures at the inner and outer targets are different thermoelectric currents appear in order to compensate the difference of sheath poten-

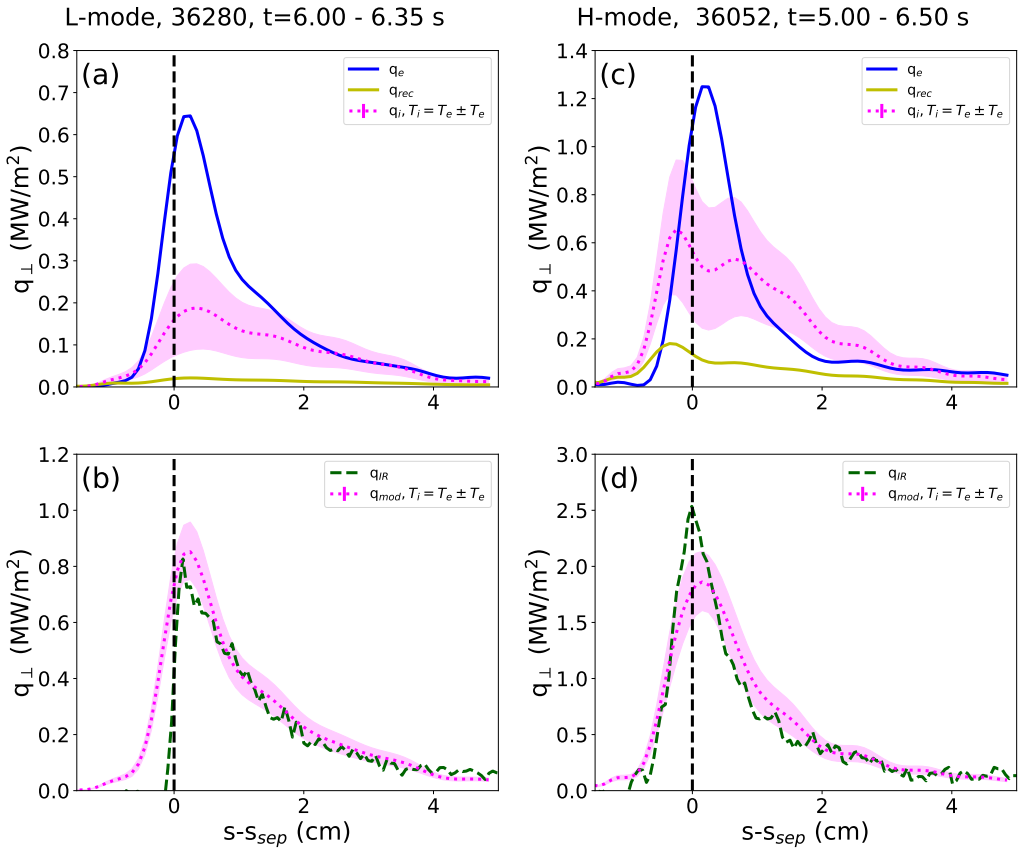

Figure 7: (a and c) Electron, ion and recombination contributions q_e, q_i and q_{rec} to the total heat flux and (b and d) comparison of modeled heat flux profile from LP data q_{mod} and IR heat flux profile q_{IR} for the L-mode discharge 36280 and the H-mode discharge 36052.

tials [3]. For zero parallel electrical resistivity this difference is compensated completely in the sheaths. Assuming a finite resistivity the potential difference is compensated partly in the SOL between the sheaths and the current is reduced compared to the model with zero resistivity. In [4] the thermoelectric current is modeled by assuming a Langmuir type model for the sheaths, finite resistivity and constant plasma pressure in the SOL, resulting in the following equation for the thermoelectric current:

$$\frac{\eta_{\parallel} L_{\parallel} j_{\mathrm{sat,in}}}{T_{e,\mathrm{in}}} \hat{j} = -\left((\kappa_{\mathrm{sh}} + \kappa_{\mathrm{presh}} - \alpha) \left(\frac{T_{e,\mathrm{out}}}{T_{e,\mathrm{in}}} - 1 \right) \right) - \ln \left(\frac{1 + \hat{j}}{\left[1 - (T_{e,\mathrm{out}}/T_{e,\mathrm{in}})^{1/2} \hat{j} \right]^{T_{e,\mathrm{out}}/T_{e,\mathrm{in}}}} \right). \tag{5}$$

Here $\hat{j} \equiv j_{\mathrm{th}}/j_{\mathrm{sat,in}}$ is the thermoelectric current j_{th} normalized to the inner target saturation current density $j_{\mathrm{sat,in}}$, $T_{e,\mathrm{out}}$ and $T_{e,\mathrm{in}}$ are the electron temperatures at the outer and inner targets, the coefficients $\kappa_{\mathrm{sh}} = 3.89$ and $\kappa_{presh} = 0.85$ are the floating and presheath potentials normalized to the target electron temperature, $\alpha = 0.7$ is the normalized temperature gradient force onto the electrons, $L_{\parallel}$ the parallel connection length between the inner and outer targets and $\eta_{\parallel}$ the averaged parallel resistivity. For an effective charge number $\mathrm{Z_{eff}} = 1$, $\eta_{\parallel}$ is given by

$$\eta_{\parallel} = 5.2 \times 10^{-5} \ln \Lambda / T_e^{3/2}, \tag{6}$$

where $\ln \Lambda$ is the Coulomb logarithm, and T_e the average electron temperature. The inner target saturation current density required to solve Eq. (5) is calculated by $j_{\mathrm{sat,in}} = n_{e,\mathrm{in}} \sqrt{2 e T_{e,\mathrm{in}}/m_i}$, where m_i is the ion mass. Due to the assumed pressure conservation, $n_{e,\mathrm{in}}$ is related to the average density n_e by $n_{e,\mathrm{in}} = n_e T_e / T_{e,\mathrm{in}}$.

By solving Eq. (5) $\hat{j}$ is obtained as a function of the ratio $T_{e,\mathrm{out}}/T_{e,\mathrm{in}}$. Figure 8 shows the solution of this equation for $n_e = 0.5 \times 10^{19}\,\mathrm{m}^{-3}$, $T_e = 60\,\mathrm{eV}$, $T_{e,\mathrm{in}} = 20\,\mathrm{eV}$ and $L_{\parallel} = 60\,\mathrm{m}$, which corresponds approximately to the parameters of the discharge 36280. The value chosen for $T_{e,\mathrm{in}}$ is the peak temperature measured by the triple probes at the inner target. For $T_{e,\mathrm{out}}/T_{e,\mathrm{in}} < 2$, j_{th} is significantly smaller than $j_{\mathrm{sat,in}}$, while for $T_{e,\mathrm{out}}/T_{e,\mathrm{in}} > 2$, which is fulfilled in the discharge 36280, j_{th} approaches to $j_{\mathrm{sat,in}}$.

For the discharge 36280 no reliable full inner target ion saturation profiles could be obtained. Instead, LP data from the L-mode discharge 34320, with similar conditions as the discharge 36280, is used for this comparison. In Fig. 9 the profiles of j_{net} measured at the outer target and $j_{\mathrm{sat,in}} f_{\mathrm{in}}^{\mathrm{out}}$ with respect to the poloidal flux coordinate ρ_p are shown. Here $f_{\mathrm{in}}^{\mathrm{out}}$ is the flux expansion between inner and outer target. The shape as well as the magnitude of both profiles are in good agreement. The negative dip in j_{net} in the PFR is caused by the diamagnetic currents, as discussed before. The agreement between the two profiles confirms that the electric current observed at the outer target is dominantly driven by the thermoelectric effect.

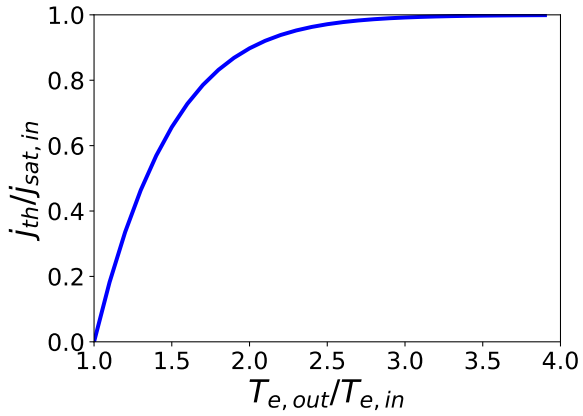

Figure 8: Ratio of the thermoelectric current j_{th} and inner target ion saturation current $j_{\mathrm{sat,in}}$ in dependence of the ratio of outer and inner target electron temperatures $T_{e,\mathrm{out}}$ and $T_{e,\mathrm{in}}$ according to Ref. [4].

The discharges discussed in the previous sections correspond to conditions where the outer as well as inner targets are attached. However, as the density is increased the outer target ion saturation current increases and the electric current decreases due to the detachment of the inner divertor. These effects should lead to a decrease of the ratio $j_{\mathrm{net}}/j_{\mathrm{sat,out}}$. To quantify this dependence a series of L-mode discharges with varying densities is analysed. The ion saturation current $j_{\mathrm{sat,out}}$ in these discharges is obtained from the flush triple Langmuir probes, and the electric current j_{net} from grounded flush probes. Figure 10 (a) shows the peak value of j_{net} and the $j_{\mathrm{sat,out}}$ value at the same target location in dependence on the edge density n_{H5}. j_{net} increases for low densities slightly, while for $n_{\mathrm{H5}} > 1.5 \times 10^{19}\,\mathrm{m}^{-3}$ it drops again. Although it should be noted that for higher densities the data is sparse, the drop of j_{net} is consistent with the picture that the thermal current decreases above a certain density due to a detaching inner divertor. j_{net} does however not reach zero, which may be explained by the aforementioned diamagnetic currents. The saturation current $j_{\mathrm{sat,out}}$ increases approximately linearly with n_{H5}. Fig. 10 (b) shows the ratio of the j_{net} and $j_{\mathrm{sat,out}}$ values from Fig. 10 (a). For the lowest densities the ratio is around 6 and decreases approximately linearly to values below one with increasing density. As is seen from Eq. (1) the importance of the electric current increases for an increasing ratio of j_{net} and $j_{\mathrm{sat,out}}$. For increasing densities the contribution of the electric current to the target heat flux becomes therefore less significant.

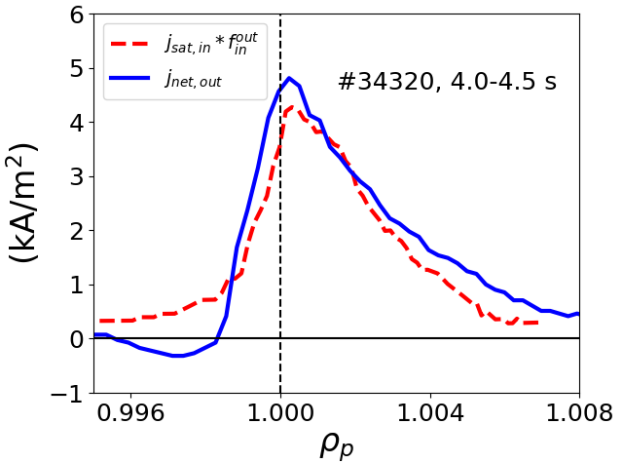

Figure 9: Inner target ion saturation current $j_{\mathrm{sat,in}}$ and outer target electric current $j_{\mathrm{net,out}}$ for the AUG discharge 34320 in dependence of the poloidal flux coordinate ρ_p.

6 Model for parallel heat transport with strong electric currents

Thermoelectric currents are carried by a flow of electrons from the colder to the hotter target, and therefore this mechanism leads to a convective heat flux. To estimate the contribution of this convective heat flux to the total electron heat flux, a one dimensional heat transport model is employed. In the model it is assumed that 1) there are no volumetric heat sources and sinks, 2) electron-ion energy exchange is negligible in the SOL. With these assumptions the following heat flux equation for the electrons is obtained from the Braginskii equation for the electron temperature [6, 30]:

$$\overbrace{-\kappa_e T_e^{5/2} \frac{dT_e}{dl}}^{q_{\mathrm{cond,e}}} + \overbrace{\left(\frac{5}{2} + 0.71\right) j_{\mathrm{net},\parallel} T_e}^{q_{\mathrm{conv,e}}} = q_{e,\parallel} \tag{7}$$

Here $q_{e,\parallel}$ is the parallel electron heat flux, $\kappa_e \approx 2400\,\mathrm{Wm/eV^{2/7}}$ for $\mathrm{Z_{eff}} = 1$ [31], and l the distance from the outer target along the field line. The terms $q_{\mathrm{cond,e}}$ and $q_{\mathrm{conv,e}}$ on the left hand side of Eq. (7) are the conductive and convective parts of the electron heat flux, respectively. The conductive term is set according to Spitzer-Härm. Both terms, $j_{\mathrm{net},\parallel}$ and $q_{e,\parallel}$, are assumed to be constant along the field line, and the outer target electron temperature $T_{e,\mathrm{out}}$ is a free input in the model.

The electron heat flux $q_{e,\parallel}$ is obtained from the probe measurements by

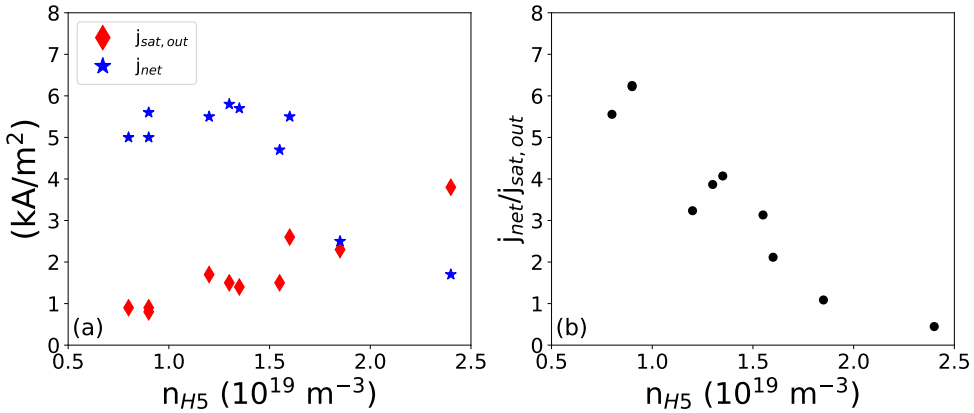

Figure 10: (a) Outer target current density j_{net} and ion saturation current density $j_{\mathrm{sat,out}}$ in dependence on the edge density n_{H5} for L-mode discharges. (b) Ratio $j_{\mathrm{net}}/j_{\mathrm{sat,out}}$ at the outer target in dependence on n_{H5}.

adding the heat flux required to overcome the potential drop of the sheath to the electron target heat flux:

$$q_{e,\parallel} = (2T_e + eV_{\mathrm{sh}})(j_{\mathrm{sat}} + j_{\mathrm{net}})/\sin(\alpha), \tag{8}$$

The factor $1/\sin(\alpha)$, where α is the angle between the magnetic field and the target plate, is required to convert perpendicular (i.e. towards the target) to parallel heat fluxes. Here $\alpha = 2.5°$ is used, which is a typical value at the outer target in AUG. The sheath drop V_{sh}, which is calculated from Eq. (3), is typically between 2 and $3T_e/e$, i.e. the upstream electron heat flux is around twice that of the target electron heat flux.

Equation (7) is solved numerically for both the L- and H-mode cases with the following parameters:

- For the L-mode discharge $T_{e,\mathrm{out}} = 60\,\mathrm{eV}$ is used (see. Fig. 4 (a)). From the LP data $q_{e,\parallel}\sin(\alpha) \approx 1.5\,\mathrm{MW/m^2}$ is obtained (see Fig. 7). To check the influence of the uncertainties, Eq. (7) is solved additionally for $q_{e,\parallel}\sin(\alpha) = 1$ and $2\,\mathrm{MW/m^2}$.

- For the H-mode discharge $T_{e,\mathrm{out}} = 30\,\mathrm{eV}$ is used (see. Fig. 4 (b)). Here Eq. (7) is solved for $q_{e,\parallel}\sin(\alpha) = 3.0$, 4.0 and $5.0\,\mathrm{MW/m^2}$.

The peak target current j_{net} is in both cases scanned between 0 and $30\,\mathrm{kA/m^2}$.

The solutions for the upstream (25 m parallel upstream away from the target) convective heat fluxes normalized to $q_{\parallel,e}$ are shown in Fig. 11 (a) as functions of j_{net}. For $j_{\mathrm{net}} = 0$ the convective part is zero, and the electron heat flux is described exactly by the Spitzer-Härm term. With increasing

j_{net} the normalized convective flux increases until it reaches unity. For the L-mode discharge the peak value of j_{net} is about $4\,\mathrm{kA/m^2}$, and, therefore, between 40 and 80 % of the total electron heat flux is carried convectively. For the H-mode discharge the peak value of j_{net} is about $15\,\mathrm{kA/m^2}$, and between 60 and 90 % is carried convectively. However, the maximum target current might be higher than the upstream current, due to the diamagnetic currents. Nevertheless, assuming that the upstream current is only half of the target current, still about 50 % is carried convectively. The convective heat flux from the colder to the hotter target also contributes to the heat flux asymmetry between the targets as discussed in Refs. [5, 6].

The upstream electron temperature T_e^u obtained from the solution of Eq. (7) is shown in Fig. 11 (b). For all solutions T_e^u is decreasing approximately linearly with j_{net}. The slope dT_e^u/dj_{net} is for all solutions about $-1\,\mathrm{eV/(kA/m^2)}$. Therefore, for $j_{\mathrm{net}} = 4\,\mathrm{kA/m^2}$ the upstream temperature is about 4 eV lower, and for $j_{\mathrm{net}} = 15\,\mathrm{kA/m^2}$ about 15 eV lower than what would be obtained by assuming pure Spitzer-Härm heat transport.

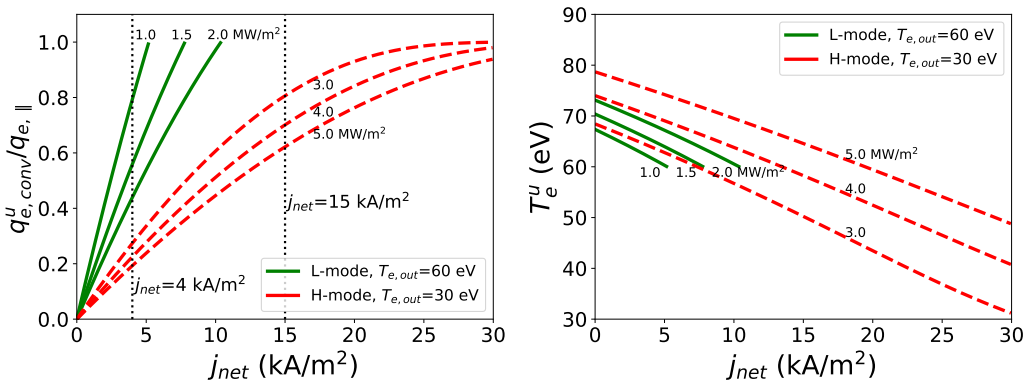

(a) (b)

Figure 11: Ratio of convective electron to total heat flux $q^u_{e,conv}/q_{e,\parallel}$ (a) and upstream electron temperature T_e^u (b) in dependence of the electric current j_{net}. Curves were obtained by solving Eq. (7).

7 Application of results: Estimation of the power decay length from LP data

Attached heat flux profiles can be well described by the model described in in [19,32]. The fitting parameters q_0, λ_q and S used in this model parametrize the upstream peak heat flux, the e-folding length of the profile, and the

spreading of the profile towards the PFR. In particular λ_q is an important quantity to predict the power exhaust capabilities in future fusion devices. A large λ_q is not only beneficial since the power spreads over a larger area, but also since the radiating volume increases [33]. To calculate the target heat flux from LP data it is commonly assumed that the target is floating. In the following it is demonstrated how this assumption influences the estimation of the heat flux profile and the corresponding fitting parameters.

Floating target conditions correspond to $V_{\mathrm{tar,fl}} = 0$ in Fig. 6 (a) and (b). With respect to $V_{\mathrm{tar,fl}} > 0$ the electron heat flux is underestimated, and the ion heat flux overestimated. Since the underestimation of γ_e is stronger than the overestimation of γ_i, the total sheath heat transmission factor decreases. Figure 12 shows for the L-mode #36280 the IR heat flux q_{IR}, the heat flux profiles obtained from the Langmuir probes with the correct sheath heat transmission factor q_{mod}, and with the assumption of a floating target $q_{\mathrm{mod,fl}}$. The fits of the profiles are shown by the solid lines. For the LP heat fluxes $T_i = T_e$ and $R_E = 0.5$ is used. The floating target assumption results in a spatially constant sheath heat transmission factor of about 5.

The power decay lengths obtained for the fit functions are about 3 mm for both q_{IR} as well as q_{mod}. For $q_{\mathrm{mod,fl}}$ the decay length is 4.1 mm. Thus with a constant sheath heat transmission factor λ_q is overestimated by about one third in this case. This is in line with the results from [34], where the power decay length obtained from LP measurements with a constant sheath heat transmission factor is systematically by a factor of about 1.3 larger than the one obtained from IR measurements.

8 Conclusions

Electric currents measured with shunt resistors in the divertor targets of AUG were previously explained by the thermoelectric effect. The Langmuir probe measurements presented here show that for low collisionality SOL conditions, the electric currents at the outer target can be several times larger than the ion saturation current for both L- as well as H-modes. The outer target electric current and the inner target ion saturation current profiles are compared for an L-mode case, and good agreement between them is found. This shows that the electrons flow from the inner to the outer target, while the inner target flow is depleted of electrons. By increasing the density the electric current decreases, while the outer target ion saturation current increases, leading to a decrease of their ratio.

Due to the strong electric currents the assumption of an ambipolar flux to each of the targets is not fulfilled. This has to be taken into account when

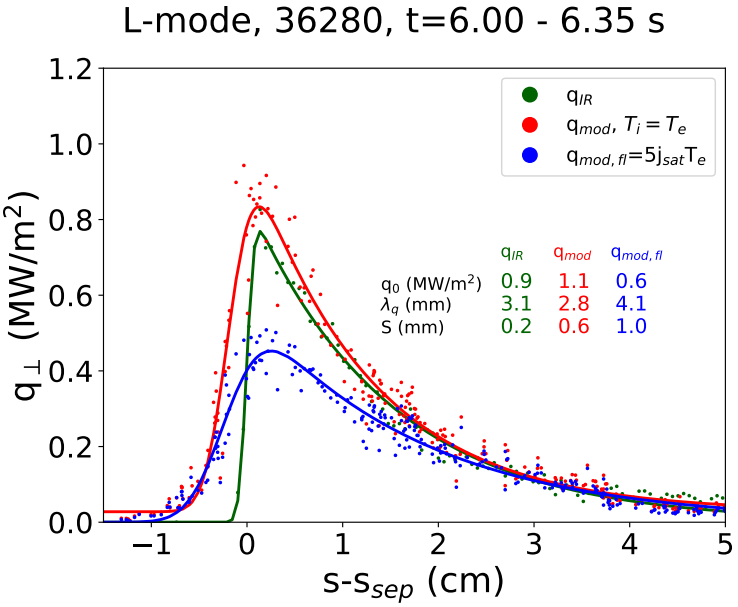

Figure 12: Outer target heat flux profiles from IR (q_{IR}), from LPs calculated according to Eq. (1) with $T_i = T_e$ and $R_E = 0.5$ (q_{mod}) and from LPs calculated with the standard formula for floating conditions ($q_{\mathrm{mod,fl}}$). The corresponding fits are obtained according to the model described in [19].

calculating the heat flux from the Langmuir probe data. The analysis of the obtained heat flux profiles shows that the ion and electron heat flux shapes differ strongly in the investigated low density discharges. In particular, including the current in the analysis leads to higher peak heat fluxes, and to smaller near SOL heat flux widths derived by the LP method.

If the ratio of electric to ion saturation current is small, the electric current can be neglected in the heat flux calculation. The assumption of a spatially constant sheath heat transmission factor does therefore not lead to large errors at high densities.

The commonly used assumption of using a pure Spitzer-Härm heat transport is inspected by setting up a simplified model including the heat transport by the electric current. Solutions of this model show that, for the experimentally observed conditions, less than 50 % of the electron heat flux might be carried by conduction. The model predicts, furthermore, that the upstream temperature drops approximately linearly with the current. For the investigated conditions this led to a drop betwen 5 and 15 eV, compared to the case with no current.

High negative target currents require the sheath potential drop V_{sh} to

decrease with respect to the commonly used approximation of $V_{\mathrm{sh}} = 3T_e/e$, which has not yet been addressed in this work. This has to be taken into account when calculating the electric fields upstream and in the divertor region from the target conditions. In particular the decreasing electric currents through increasing density, might affect the upstream radial electric field and its shear, and thereby have an effect on the L-H transition and blob transport. Analysing the upstream electric field with regards to SOL currents, and its further effects will be the subject of future work.

9 Acknowledgements

This work has been carried out within the framework of the EUROfusion Consortium and has received funding from the Euratom research and training programme 2014-2018 and 2019-2020 under grant agreement No 633053. The views and opinions expressed herein do not necessarily reflect those of the European Commission.

References

[1] T. Eich et al. Scaling of the tokamak near the scrape-off layer H-mode power width and implications for ITER. *Nucl. Fusion*, 53(9):093031, 2013.

[2] A.V. Chankin. Classical drifts in the tokamak sol and divertor: models and experiment. *Journal of Nuclear Materials*, 241-243:199 – 213, 1997.

[3] P. J. Harbour. Current flow parallel to the field in a scrape-off layer. *Contributions to Plasma Physics*, 28(4-5):417–419, 1988.

[4] G. M. Staebler and F. L. Hinton. Currents in the scrape-off layer of diverted tokamaks. *Nucl. Fusion*, 29(10):1820, 1989.

[5] V. Rozhansky et al. Contribution of $\vec{E} \times \vec{B}$ drifts and parallel currents to divertor asymmetries. *Nuclear Fusion*, 52(10):103017, sep 2012.

[6] B. Labombard et al. Experimental investigation of transport phenomena in the scrape-off layer and divertor. *Journal of Nuclear Materials*, 241-243:149 – 166, 1997.

[7] D. Brunner and B. LaBombard. Surface thermocouples for measurement of pulsed heat flux in the divertor of the alcator c-mod tokamak. *Review of Scientific Instruments*, 83(3):033501, 2012.

[8] S. Marsen et al. 40. EPS Conf. on Plasma Physics (2013), Espoo, Finland, p1.127.

[9] A. Kallenbach et al. Electric currents in the scrape-off layer in ASDEX Upgrade. *J. Nucl. Mater.*, 290:639–643, 2001.

[10] A. Kallenbach et al. Divertor power load feedback with nitrogen seeding in ASDEX Upgrade. *Plasma Phys. Control. Fusion*, 52(5):055002, 2010.

[11] A. Bergmann. Two-dimensional particle simulation of Langmuir probe sheaths with oblique magnetic field. *Physics of Plasmas*, 1(11):3598–3606, 1994.

[12] G. F. Matthews et al. Investigation of the fluxes to a surface at grazing angles of incidence in the tokamak boundary. *Plasma Physics and Controlled Fusion*, 32(14):1301–1320, dec 1990.

[13] M. Weinlich and A. Carlson. Flush mounted langmuir probes in an oblique magnetic field. *Physics of Plasmas*, 4(6):2151–2160, 1997.

[14] M. Komm et al. On attenuation of electron current of flush-mounted probes and electrodes in magnetised plasmas. *Nuclear Fusion*, 59(9):096050, aug 2019.

[15] M. Weinlich and A. Carlson. Flush mounted probes in ASDEX Upgrade - can they be operated as triple probes? *Contrib. Plasma Phys.*, 36(S1):53–59, 1996.

[16] B. Sieglin et al. Real time capable infrared thermography for ASDEX Upgrade. *Rev. Sci. Instrum.*, 86(11):113502, 2015.

[17] D. Nille et al. Probabilistic inference of surface heat flux densities from infrared thermography. In *Bayesian Inference and Maximum Entropy Methods in Science and Engineering*, pages 55–64, Cham, 2018. Springer International Publishing.

[18] A. Herrmann et al. Energy flux to the ASDEX Upgrade diverter plates determined by thermography and calorimetry. *Plasma Phys. Control. Fusion*, 37(1):17, 1995.

[19] T. Eich et al. Inter-ELM power decay length for JET and ASDEX Upgrade: Measurement and comparison with heuristic drift-based model. *Phys. Rev. Lett.*, 107:215001, Nov 2011.

[20] A Scarabosio et al. Scaling of the divertor power spreading (S-factor) in open and closed divertor operation in JET and ASDEX Upgrade. *Journal of Nuclear Materials*, 463:49–54, 2015.

[21] L. Aho-Mantila. Outer divertor of ASDEX Upgrade in low-density L-mode discharges in forward and reversed magnetic field: I. comparison between measured plasma conditions and SOLPS5.0 code calculations. *Nuclear Fusion*, 52(10):103006, 2012.

[22] M. Bernert et al. The H-mode density limit in the full tungsten ASDEX Upgrade tokamak. *Plasma Physics and Controlled Fusion*, 57(1):014038, nov 2014.

[23] James P Gunn et al. Flush-mounted probes in the divertor plates of Tokamak de Varennes. *Review of scientific instruments*, 66(1):154–159, 1995.

[24] M.J. Schaffer, A.V. Chankin, H.Y. Guo, G.F. Matthews, and R. Monk. Pfirsch-Schluter currents in the JET divertor. *Nuclear Fusion*, 37(1):83–99, jan 1997.

[25] V. Rozhansky et al. Potentials and currents in the edge tokamak plasma: simplified approach and comparison with two-dimensional modelling. *Nuclear Fusion*, 43(7):614–621, jul 2003.

[26] P. C. Stangeby et al. *The Plasma Boundary of Magnetic Fusion Devices*. Institute of Physics Publishing Bristol, 2000.

[27] W. Eckstein. Reflection (Backscattering), Technical Report IPP 17/12, 2009.

[28] D. Tskhakaya and S. Kuhn. Influence of initial energy on the effective secondary-electron emission coefficient in the presence of an oblique magnetic field. *Contrib. Plasma Phys.*, 40(3-4):484–490, 2000.

[29] D. Brida et al. Heat flux pattern in detached L-modes and ELM mitigated H-modes with rotating magnetic perturbations in ASDEX Upgrade. *Nuclear Fusion*, 57(11):116006, 2017.

[30] S.I. Braginskii. Transport processes in a plasma. *Rev. Plasma Phys.*, 1:205, 1965.

[31] R.J. Goldston et al. A new scaling for divertor detachment. *Plasma Physics and Controlled Fusion*, 59(5):055015, 2017.

[32] F. Wagner. *Nucl. Fusion*, 25(5):525, 1985.

[33] A. Kallenbach et al. Multi-machine comparisons of divertor heat flux mitigation by radiative cooling. Technical report, 2012.

[34] L. Wang et al. Scaling of divertor power footprint width in RF-heated type-III ELMy H-mode on the EAST superconducting tokamak. *Nuclear Fusion*, 54(11):114002, nov 2014.